JGR Solid Earth

RESEARCH ARTICLE

Key Points:
- Local earthquake tomography maps a low-velocity anomaly offshore the Tjörnes Fracture Zone
- A curvilinear gravity low coincides with the low-velocity anomaly

Correspondence to:
C. Abril,
cyabrill@gmail.com

Local Earthquake Tomography in the Tjörnes Fracture Zone (North Iceland)

C. Abril[1,2] , **A. Tryggvason[1]**, **Ó. Gudmundsson[1]**, and **R. Steffen[1,3]**

[1]Department of Earth Sciences, Uppsala University, Uppsala, Sweden, [2]Icelandic Meteorological Office - IMO, Reykjavík, Iceland, [3]Lantmäteriet, Gävle, Sweden

Abstract Local earthquake tomography has been carried out in the Tjörnes Fracture Zone. This transform region connects the Mid-Atlantic Ridge to the Northern Volcanic Zone in Iceland in a mostly offshore area. The challenge to record seismic information in this area was the motivation for the North ICeland Experiment (NICE). Fourteen ocean-bottom seismometers and eleven on-land stations were installed in the project and operated simultaneously with the permanent Icelandic seismic network (SIL) during summer 2004. Data from the experiment were used to estimate P- and S-wave crustal velocities. Also, the gravity anomaly was derived for comparison with the tomographic results. Upper-crustal velocities are found to be relatively low in the offshore region. In particular, low velocities are mapped along the Húsavík-Flatey Fault, where a more confined negative gravity anomaly and a sedimentary basin are found. Low velocities are also mapped along the Grímsey Oblique Rift and in a zone connecting these two main lineaments. The northern half of the aseismic Grímsey Shoal appears as a fast anomaly. Furthermore, localized high-velocity anomalies are found beneath northern Tröllaskagi and Flateyjarskagi Peninsulas, where bedrock dates from Upper and Middle Miocene (10–15 Ma). Regions of low Vp/Vs ratios are mapped at depth along the main lineaments. Low velocities along the lineaments are interpreted as due to fracturing extending into the middle crust, while high velocities in the upper crust beneath Tertiary formations are associated with relic volcanoes. Low Vp/Vs variations along the lineaments are interpreted as due to the presence of supercritical fluids.

Plain Language Summary We studied the crustal structure in Tjörnes Fracture Zone (North Iceland) by carrying out an earthquake tomography. As a result, we generated velocity models for seismic waves. This study has the particular advantage of including earthquakes recorded by seismic stations deployed offshore in the zone. It allowed us to get detailed information from areas difficult to cover with the permanent Icelandic seismic network, whose instruments are located on-land. Additionally, we estimate the gravity anomaly in the area for its comparison with the velocity models. We found low velocities at shallow layers offshore, specifically along the Húsavík-Flatey Fault, where a negative gravity anomaly is located. Low velocities are also found in the Grímsey Oblique Rift. We interpret the low velocities as a consequence of the presence of sediments and the fracturing of rocks. In contrast, we found fast velocities at the Grímsey Shoal and beneath the Tröllaskagi and Flateyjarskagi Peninsulas. We interpret those velocities as due to the presence of Tertiary rocks associated with relic volcanoes.

1. Introduction

The Tjörnes Fracture Zone (TFZ) is a transform zone that connects the Kolbeinsey Ridge (KR) to the Northern Volcanic Zone (NVZ) of Iceland. The TFZ has two main sub-parallel structures approximately oriented SE-NW: the Húsavík Flatey Fault (HFF) and the Grímsey Oblique Rift (GOR). Additionally, the KR continues to the south as the Eyjafjarðaráll Rift (ER) on the western border of the TFZ. Together these parts of the TFZ demark the Tjörnes Microplate (TM) (see Figure 1). The HFF, the GOR and the ER encompass most of the seismicity in the region (Figure 2). The seismicity of the area is characterized by the SIL earthquake catalog of the Icelandic Meteorological Office (IMO) (Bödvarsson et al., 1999; Rögnvaldsson et al., 1998).

The HFF is a WNW-striking, right-lateral strike-slip fault that extends from the Þeistareykir fissure swarm in the NVZ to the southern end of the ER. The eastern part of the HFF is a set of subparallel faults located on land on the Tjörnes Peninsula. The central and western parts are located offshore (Figure 1). The ER is a pull-apart basin characterized by a semi-symmetric pattern of normal faulting on a north-striking axis
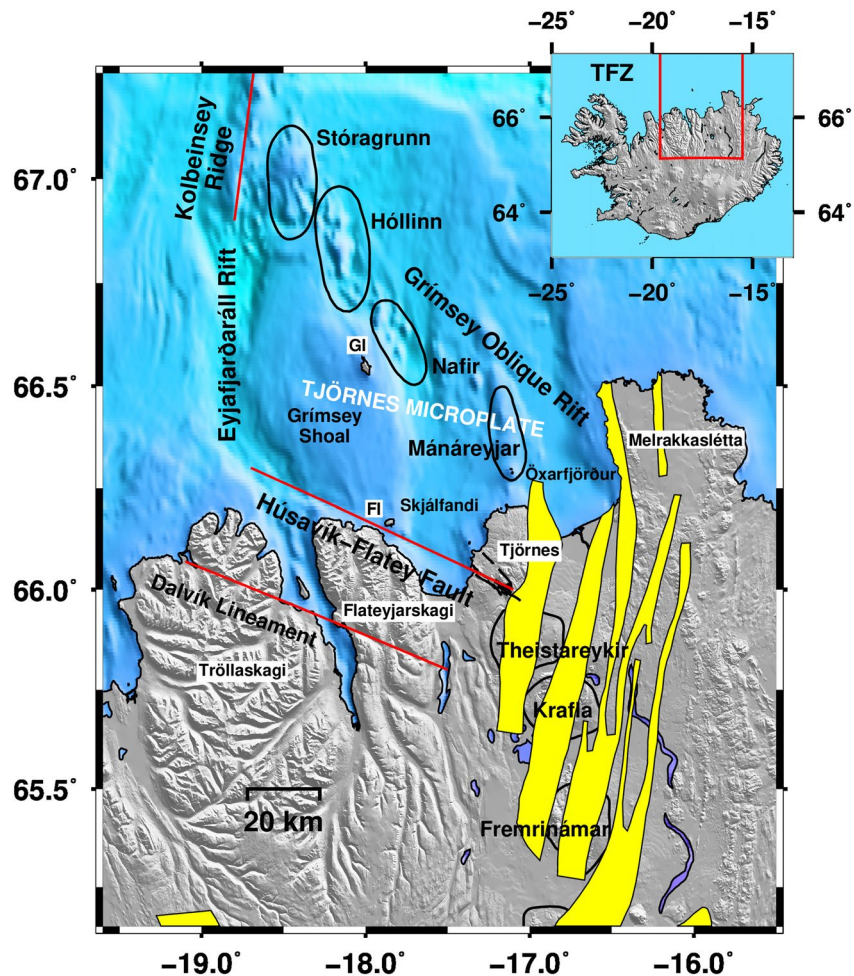
Figure 1. Map of Northern Iceland. The Tjörnes Fracture Zone connects the Kolbeinsey Ridge to the Northern Volcanic Zone and its volcanic centers (Þeistareykir, Krafla and Fremrinámar are shown here). The main tectonic structures of the TFZ are the Húsavík-Flatey Fault, the volcanic centers in the Grímsey Oblique Rift and the Eyjafjarðaráll Basin. An outline of the suggested Dalvík Lineament is also shown. Volcanic centers are outlined with black rings. Yellow corridors correspond to fissure swarms. Black labels on white boxes are used to indicate Tröllaskagi, Flateyjarskagi, Tjörnes and Melrakkaslétta Peninsulas. We use the same convenction to indicate the location of the Flatey (FI) and Grímsey (GI) Islands. Peninsulas and Islands are presented for geographic reference. The upper inset shows the location of the TFZ in Iceland.

(Gunnarsson, 1998). The basin widens to the south near the HFF in a corridor ~20 km wide. Evidence for recent volcanism is scarce (Einarsson, 2008). The ER connects to the GOR in the north, a lineament that is subparallel to the HFF. The GOR is composed of four volcanic systems arranged *en echelon* and oriented NS to NNW-SSE (Magnúsdóttir et al., 2015; Rögnvaldsson et al., 1998), and transverse (NNE striking) strike-slip faults. The GOR connects to the Krafla fissure swarm at its eastern end. Evidence of recent volcanism in the GOR is abundant. The last eruptive activity occurred within the Mánareyar volcanic system in 1867–1868 (Sæmundsson, 1973).

Other lineaments associated with the TFZ have less frequent earthquakes compared to the HFF and the GOR. The Dalvík Lineament (DL), located south of the HFF, is where some of the largest historic earthquakes have occurred. For example, the 1934 $M = 6.3$ and the 1963 $M = 7.0$ earthquakes occurred there (Stefansson, 1979). Transverse lineaments, connecting the HFF to the GOR, have previously been suggested by Rögnvaldsson et al. (1998) and later supported by the earthquake relocations of Abril et al. (2018).

The SIL data have also been used to define the crustal structure in Northern Iceland. Darbyshire et al. (2000) generated teleseismic receiver functions at broadband stations of the SIL network. In general, receiver
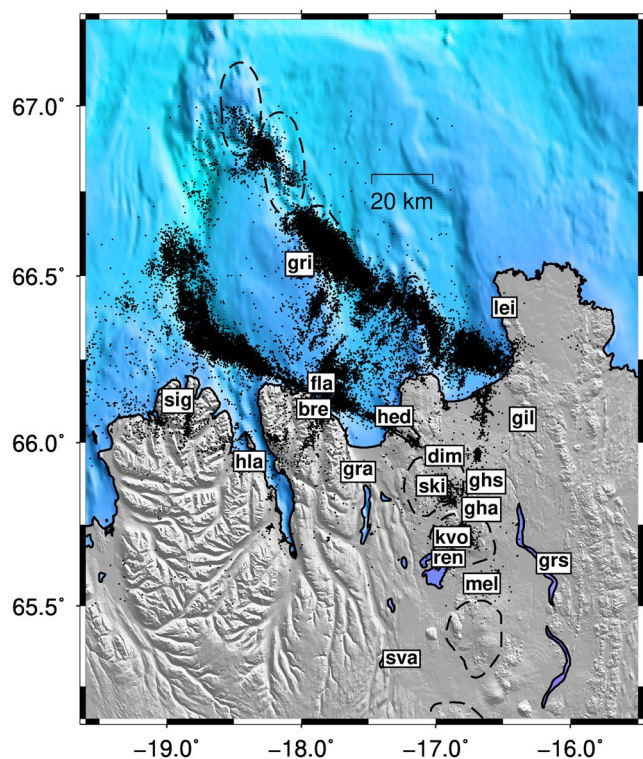
Figure 2. Seismicity in Northern Iceland recorded by the SIL network from 1993 to 2017 (black dots) and the distribution of SIL stations during the NICE experiment (summer 2004). Station names are presented in white boxes. Volcanic centers in the Northern Volcanic Zone and the Tjörnes Fracture Zone are outlined with dashed rings.

functions evidenced a strong lateral heterogeneity in the crustal structure of the region. A crustal thickness of 20–22 km was estimated to the southeast near the Northern Volcanic Zone (stations REN and GRA), while a thicker crust of 25–30 km was modeled for stations GIL and SIG (see stations' location in Figure 2). A thinner crust of about 16 km was reported for the insular area (GRI) (see Figure 2). Riedel et al. (2005) performed a travel-time inversion using data from the SIL catalog. Assuming a maximum crustal velocity of 7.4 km/s, the crustal thickness was estimated to be 20 km at HFF and 8 km at the GOR.

As most of the TFZ is located offshore, available seismological and geological data collected on land provide limited information. However, some studies have collected and/or used offshore information about the TFZ. Gunnarsson (1998) reported thick sediments (approximately up to 4 km thick) along the HFF and around the ER, based on data from several campaigns of seismic reflection acquisition. Magnúsdóttir et al. (2015) used multi-beam bathymetry and high-resolution seismic reflection data (CHIRP) to study the area arround the Nafir volcanic system in the GOR. Correlation with tephrochronology from the sediment core MD99-2275 near Grímsey Island provided evidence of postglacial tectonic and volcanic activity along the lineament (Gudmundsdóttir, 2010; Søndergaard, 2010).

The North ICeland Experiment (NICE) was a temporary deployment of on-land and offshore seismological instruments to record data simultaneosly with the SIL network during the summer of 2004. The main purpose was to resolve the subsurface structure of the TFZ and study the transition from the Icelandic crust to more typical oceanic crust near the southern end of the Kolbeinsey Ridge (Riedel et al., 2006). In addition, to the seismological deployment, bathymetric mapping was performed, improving the resolution of previously available data. Structures in between Hóllinn and Stóragrunn volcanoes in the GOR were revealed (Magnúsdóttir et al., 2015). Hensch et al. (2008) identified and located three earthquake swarms that occurred during the NICE deployment. Location of those swarms together with five swarms previously recorded by the SIL network suggested two different physical mechanisms: Magma propagation for the purely volcanic swarms, and hydrothermal activity and/or tectonic processes for swarms located outside the volcanic centers.

Here we analyze data from the NICE project further in order to study the TFZ. We present the results of a Local Earthquake Tomography (LET) using 500 events (earthquakes and explosions) recorded during the span of the project. We also estimate the Bouguer anomaly from free-air gravity data in the region for comparison with the tomographic results.

2. Data

The seismicity of the TFZ has been monitored with the SIL network since 1993 (Bodvarsson et al., 1996; Bödvarsson et al., 1999), recording more than 85,000 earthquakes in Northern Iceland. Earthquakes are monitored by stations located on the Icelandic coast, one station on Grímsey Island and one on Flatey Island (see Figure 2). The station distribution of the SIL network on-land renders locations of offshore earthquakes in the TFZ inaccurate. A large azimuthal gap, often greater than 180°, affects the epicenter's estimate and large distances to the nearest stations (often exceeding 10 km) do not allow a precise estimate of focal depth (Hensch et al., 2013). This uncertainty in location parameters affects the resolution of tomographic studies using only the SIL catalog. Additionally, the sparse distribution of the SIL stations only allows illumination of the crust at depths from 7 to 12 km (Riedel et al., 2005).

During the NICE project, 14 ocean-bottom seismometers (OBS) and 11 land stations were deployed in the summer of 2004 to operate simultaneously with the SIL network and record the seismicity of northern
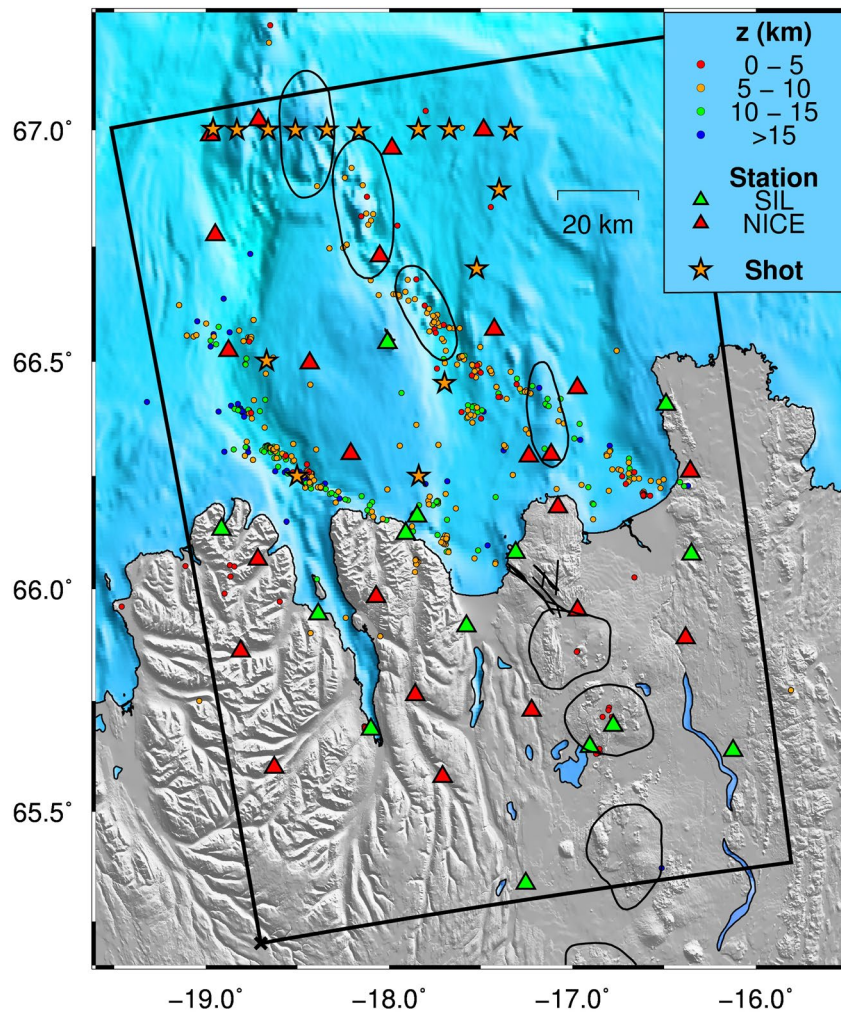
Figure 3. Distribution of seismic stations during the NICE experiment. Green triangles are the permanent SIL network stations. Red triangles are OBSs and additional on-land stations installed for the experiment. Four hundred eighty-four earthquakes (colored circles) together with the 16 shots (yellow stars) fired during the experiment were used in the LET. Earthquake locations are those estimated using the manual picking of P- and S-wave arrivals in SEISAN. The black rectangle outlines the study area. This is the area that will be used to present results in this paper, using a Cartesian coordinate system with origin in the southwestern corner of the black box (marked with a black cross). Volcanic centers are outlined with black rings.

Iceland (see Figure 3). Sixteen explosions of 22.8–45.6 kg dynamite were fired in the water column and recorded (Riedel et al., 2006). They provided ray-paths in areas of the northern TFZ that are seismically quiet. The temporary station distribution extended the coverage area of the SIL network, which allows more accurate locations of the offshore seismicity and, in particular for earthquake tomography, illuminating also the upper-most crust, which was not covered by the SIL network alone.

A waveform database was created with data from the NICE and the SIL networks recorded during the simultaneous deployment, in order to facilitate a joint analysis and phase picking. Continuous records of the NICE stations, after correction of the OBS data for clock drift (Riedel et al., 2006), were converted from the GSE (Global Seismic Exchange) to the SEISAN format (Havskov & Ottemöller, 1999). Independently, waveforms in the SIL catalog of earthquakes located in Northern Iceland were converted from SIL to SEISAN format. All the records were re-sampled to 100 Hz.

From the set of more than 1000 earthquakes used by Hensch et al. (2008), we selected a subset of 484 earthquakes and the 16 explosions (see Figure 3) such that geographical spread was maximized. Arrival times of
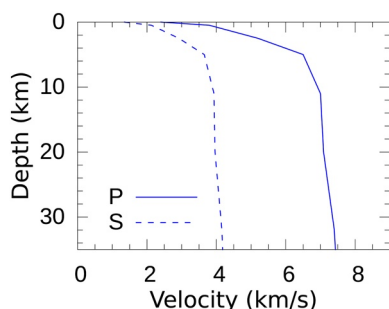
Figure 4. 1-D velocity model (Riedel et al., 2005) used for initial earthquake location after manual picking of arrivals using SEISAN.

the selected earthquakes were manually picked using SEISAN (Havskov & Ottemöller, 1999). We recognized multiple P- and S-wave arrivals in some records, where we chose to pick the first arrival of each kind without distinguishing their specific ray-path geometry (direct or refracted). The final result of manual picking was a database of approximately 5500 P-wave arrivals and 7000 S-wave arrivals, that was used as input for the LET.

To locate earthquakes with the manual picks, we used the velocity model currently used for earthquake location of events in north Iceland in the SIL catalog. This model is an average one-dimensional (1-D) velocity model estimated by Riedel et al. (2005) using travel-time inversion (see Figure 4). A constant Vp/Vs ratio of 1.78 is assumed for this model, corresponding to the average value estimated by Riedel et al. (2005).

3. Local Earthquake Tomography (LET)

We used the program PStomo$_{eq}$ to carry out the LET (Tryggvason, 1998; Tryggvason et al., 2002). PStomo$_{eq}$ performs a simultaneous inversion for P- and S-wave velocity structure and the hypocentral parameters of local earthquakes. Controlled sources with fixed locations may be used as well (Tryggvason, 1998). Travel times in PStomo$_{eq}$ are computed with the *time3d* finite-difference algorithm (Podvin & Lecomte, 1991; Tryggvason & Bergman, 2006), which computes the time field from a source (or station) to all cells in the model. The algorithm is an application of Huygens' principle using a first order approximation of the Eikonal equation. The travel times to all receivers (or sources) are computed from the resulting time field and ray tracing is performed backwards perpendicular to the isochrons (Hole, 1992). In the first step, the algorithm solves for only hypocentral parameters and then projects them out of the joint problem using the decomposition method by Pavlis and Booker (1980). Slowness perturbations are determined with the conjugate gradient solver *LSQR*, that is well suited for solving large and sparse systems of linear equations (Paige & Saunders, 1982). The tomography iteratively maps travel-time anomalies into slowness perturbations along ray paths such that new ray paths are computed in each iteration.

3.1. Starting Velocity Model and Inversion Procedure

The primary role of the starting model and initial earthquake locations is to provide ray-paths that are reasonably close to the true ones, avoiding that the linearized LET scheme will be trapped in a local minimum. Initial earthquake locations were estimated using the 1-D velocity model by Riedel et al. (2005) (see Figure 4), and the same model was used as a starting model for the LET. Several other 1D starting models were tested, but also simple 2D and 3D models accounting, for example, for the large variations in crustal thickness in the area. The crustal thickness varies from 26 km west of the Northern Volcanic Zone (Menke et al., 1998), to 16 km underneath Grímsey Island (Darbyshire et al., 2000) and 7.5 km beneath the Kolbeinsey Ridge (Kodaira et al., 1997). However, none of these models provided better final 3D P- and S-wave models in terms of RMS data fit. Thus, for simplicity we chose to use the 1D starting P- and S-wave models with a constant Vp/Vs ratio. Model cells of 0.75 km thickness and 3 km width in the horizontal were used in both models. Both larger and smaller cells were tested, but this discretization in combination with the applied model regularization appeared to reflect the model fidelity supported by the data.

3.2. Model Regularization

Regularization was applied in the inversion to minimize model artifacts (Aster et al., 2005). Smooth models were favored by pushing the Laplacian of the velocity models toward zero. In addition to this, the models were constrained by forcing the cross-gradients function between the P- and the S-wave model to be zero (Tryggvason & Linde, 2006). The cross-gradients function is the length (scalar valued) of the cross product of the velocity gradients (3D-vectors) in the P- and S-wave models at every grid node. This assures that the P- and the S-wave models are structurally similar, which implies that velocity changes in the P- and S-wave models should occur in the same location. A change, for example, in lithology affects velocities of both types
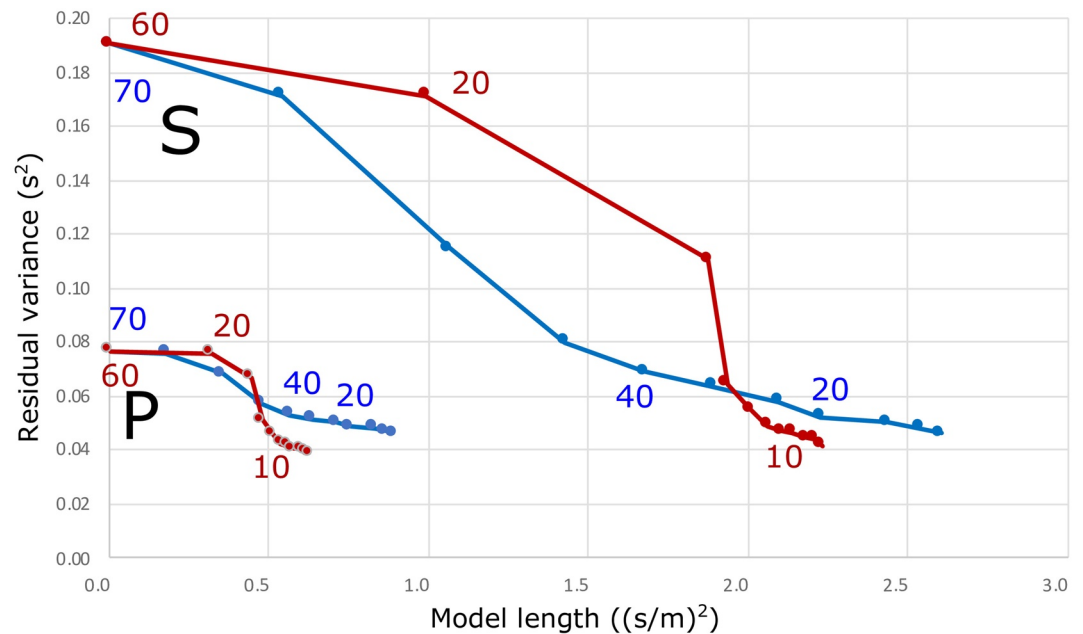
Figure 5. The progression of the inversion shows a reduction in the residual data variance versus an increase in model length. The red curves show the P- and S-wave progression starting from a 1D model (zero model length) for the models shown, utilizing cross-gradients constraints. The blue curves show the progression with an inversion with a fixed Vp/Vs ratio. The final models with the fixed Vp/Vs ratio is not able to fit the data equally well as the models allowing the Vp/Vs ratio to vary. Colored numbers next to the points on the curves show the values of the weighting on the smoother applied to inhibit wild velocity variations. The smoother is gradually relaxed as the inversion progresses.

of waves, but may change them differently. The cross-gradient function is not affected if one of the velocities increases and the other decreases. By using this constraint we found that there is no need to damp the Vp/Vs ratio, which is commonly done to avoid "wild" Vp/Vs variations, without steering the models toward a prior Vp/Vs ratio.

The course of inversion was run over 12 iterations in which the first is a plain relocation of all events in the starting models. Figure 5 shows the progression of the inversion in terms of residual-variance reduction versus model length. There are separate curves for the P- and S-wave data and models. The weight on the model regularization (the Laplacian) is relaxed (the colored number next to the points in the curves) as the inversion progresses. As the problem is nonlinear, the data fit improves also at iterations between changes in the regularization. The model length is the deviation (squared) of each effective model cell from the mean one-dimensional velocity profile. Note that the inversion is done for slowness (the inverse of velocity). The red curves are for the inversion with cross-gradients constraints (Tryggvason & Linde, 2006), and the blue curves for an inversion with a fixed Vp/Vs ratio. As Figure 5 clearly shows, a model not allowing a 3D variation of the Vp/Vs ratio cannot fit the data to the same level as an inversion allowing a 3D Vp/Vs ratio variation, despite a more complicated model (larger model length).

3.3. Residuals

The LET reduced the travel-time residuals of P- and S-wave arrivals compared to the initial 1D model. Residuals before and after the LET are shown in Figure 6. Note that all events are initially relocated in the starting model. Residuals for S-wave arrival times (blue) tend to be bigger than those for P-waves (red) which may reflect that S-wave arrivals are more difficult to determine by manual picking. At the same time, the S-wave residuals are expected to be larger than the P-wave residuals as their travel times are longer. Figure 6a also indicates that the P-wave residuals are fairly well centered on zero, suggesting that the starting model is unbiased. The S-wave residuals, on the other hand, are slightly biased to the positive side suggesting that the S-wave starting model is slightly slow. Figure 6b shows residuals after the LET in the final 3-D velocity models. The width of the residual distribution (one standard deviation) is significantly reduced by
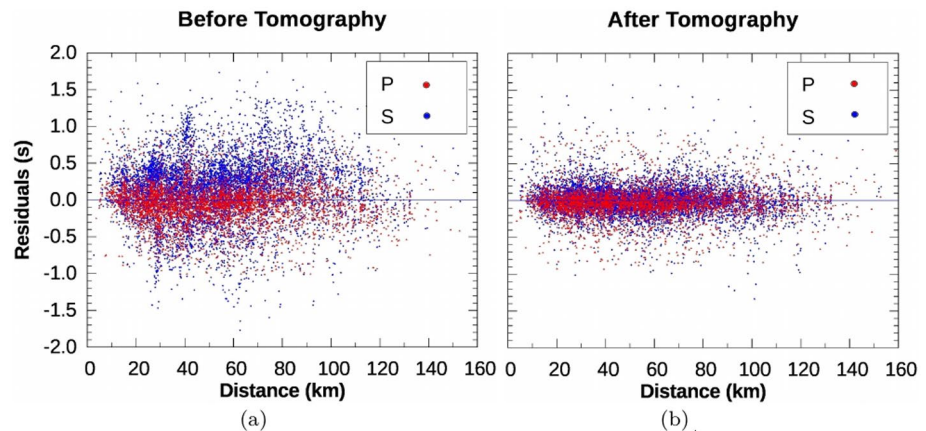
Figure 6. Residuals of P- (red dots) and S-wave (blue dots) arrival times as a function of hypocentral distance (a) before LET and (b) after LET.

the tomography from 0.28 to 0.20 s (29% reduction) for the P-waves and from 0.47 to 0.21 s (55%) for the S-waves. The mean value of the distribution is shifted toward zero, from −0.03 to 0.01 s for P-waves, and from 0.17 to 0.02 s for S-waves. The residual variance reduction is shown in Figure 5, demonstrating very little improvement beyond the 12th iteration, without increasing the model length.

3.4. Model Appraisal

The ray coverage provides an overview of how the seismic data illuminate the different parts of the model. Figure 7 shows the ray coverage through the models. The map view shows good horizontal ray coverage in the marine parts of the study area south of Grímsey. Ray coverage extends predominantly from the top 3–4–15 km depth. In addition, different tests have been carried out to appraise the model. Initially, a checkerboard test contributed to obtain a general idea about the resolution of the final 3-D velocity model (see Section 3.4.1). In the end, some of the main features of the final models were tested using hypothesis tests (see results in Section 4.1). Map views shown in this and the following sections are restricted to the study area, represented by the black rectangle drawn in Figure 3. Cartesian coordinates are used as the reference coordinate system.

3.4.1. Checkerboard Test

Checkerboard tests were conducted to estimate which regions are resolved by the experimental geometry. First, a checkerboard model was generated by superposing checkers of alternating perturbation (±10%) on top of the 1D starting P- and S-wave velocity models. Each checker was a pillar of 7 model cells across in the horizontal direction (21 × 21 km). Synthetic travel times were computed through this model. Starting from an unperturbed model, the synthetic travel times were then inverted with the same inversion parameters as used in the inversion of the real data. To make the test more challenging, the checkers were of opposite signs in the P- and S-models, and the source locations were randomly redistributed, to include also the difficulty of not knowing the exact source locations. A test where the P- and S-wave checker perturbations have opposite signs is a rather difficult test, though maybe not realistic. We note here that the cross-gradients function allows the Vp/Vs ratio to be well reconstructed as there is no constraint damping of the Vp/Vs ratio except in the
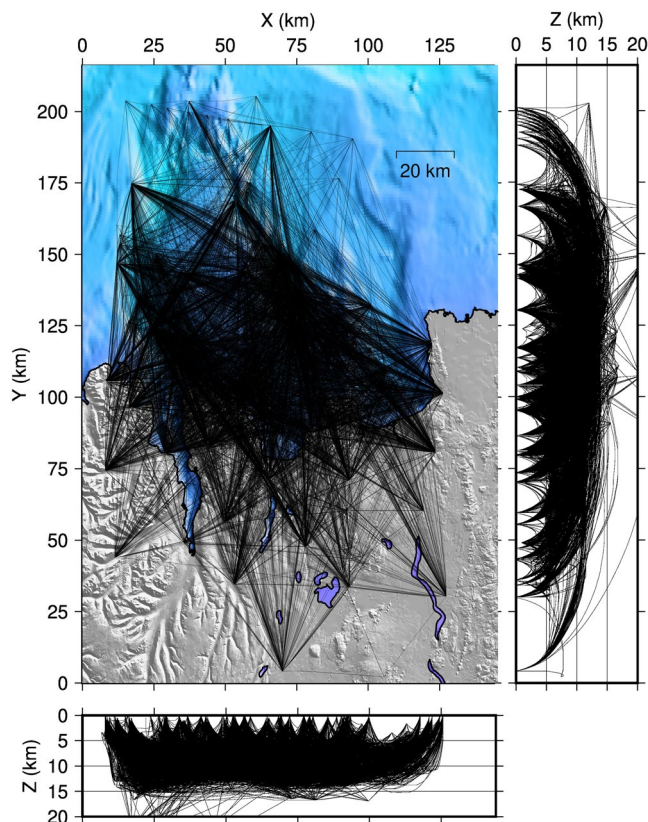

Figure 7. Ray coverage of P- and S-waves, presented in a map view and lateral views over the depth (Z).
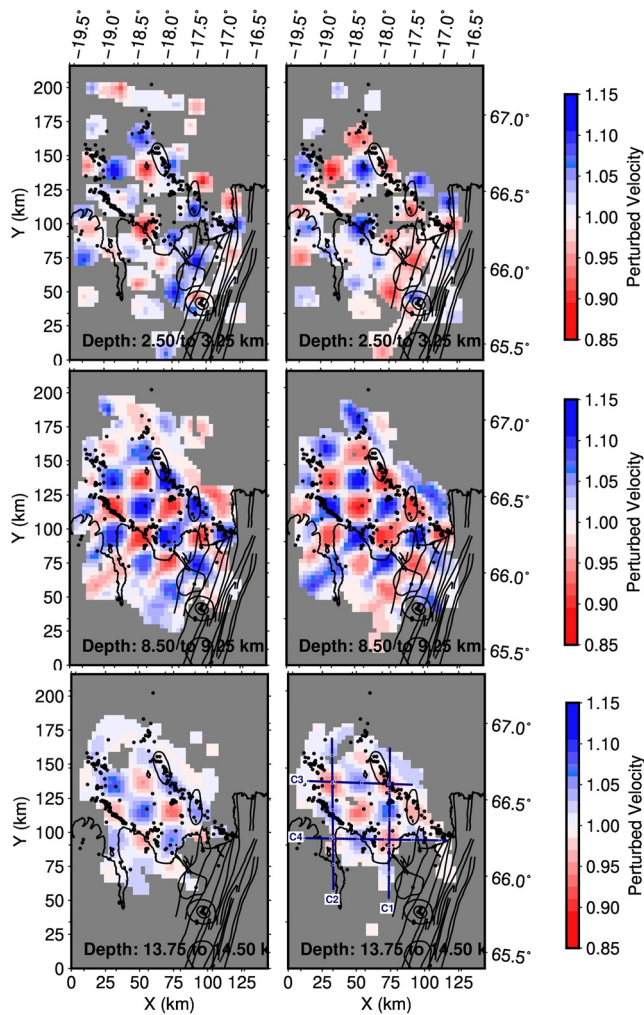
Figure 8. Checkerboard test at 2.5–3.25 km (upper panels), 8.50–9.25 km (central panels), and 13.75–14.50 km. Left panels show perturbations on the P-wave velocity model, and right panels show perturbation on the S-wave velocity model. Lower panel to the right shows the map view location of the cross sections presented in Figure 9.

initial iterations. In an otherwise identical test where the checkers have similar sign in the P- and S-wave models (not shown), the reconstruction is slightly better. This 2D checkerboard test was generated to assess and compare the resolution at different depths. The resolution is limited in some areas of the region except in the central GOR and the Flateyjaskagi Peninsula as shown by the slice at 2.5–3.25 km depth (see Figure 8). From 3.25 to 14.50 km, checkerboards show a good resolution in the central areas of the TFZ. However, checkers under 13.75 km depth only partially recover the perturbation's amplitude.

A second checkerboard test with checkers also varying in depth was generated to assess the vertical smearing. This time the perturbation was only ±5% and checkers were identical for P- and S-models. Figure 9 presents the results of this test at four different cross-sections located as shown in the lower-right panel of Figure 8. The checkers are in general well reconstructed between 5 and 13 km. There is some vertical smearing in the fringes of the model, but fairly limited in the central parts of the models where the checkers are generally well reconstructed. It should be pointed out that features much smaller than the checkers will not be correctly modeled. In regions where the checkers are fairly sharp, we argue that the resolution is on the order of a quarter of a checker and smaller features will not be correctly represented. In other regions where the smearing is more substantial, the resolution is instead on the same order as the checkers. We also observe in Figure 9 a tendency that the full strength of slow checkers are slightly more difficult to recreate than the fast checkers, as rays try to avoid them. This is likely also true for real features in the models.

4. Results

The local earthquake tomography (LET) results include models of the distribution of P- and S-wave velocity, the Vp/Vs velocity ratio, as well as relocations of the earthquakes used. We present depth slices of the final P- and S-wave velocity models between depths of 3.25 and 12.25 km in Figures 10 and 11. Three cross-sections and their respective locations are presented in Figure 12. Two of the cross-sections (P1 and P2) are along the main lineaments, the HFF and the GOR. The third (P3) is almost perpendicular to them, crossing the HFF near Flatey Island. Cells with an accumulated length of all ray-paths crossing them of less than 8.5 km (twice the length of the cell diagonal) have been masked gray in Figures 10–12. The robustness of several of the main anomalies is examined by hypothesis testing described in Section 4.1. Locations of the earthquakes used in the tomography are shown as black dots in Figures 10–12. In addition to the tomographic results, we have also analyzed gravity anomalies in the study region. The derivation of the Bouguer gravity anomaly is described in Section 4.2.

The velocity structure of the study area is illuminated approximately between 3 and 15 km depth near the main lineaments (the HFF and the GOR), and the southern ER. This is also where resolution is the highest (~11 km in horizontal direction and ~4 km in depth). In between the main lineaments, earthquakes are less frequent and relatively few earthquakes were recorded during the NICE experiment. Consequently, the ray path coverage is sparser there at shallow depths (see Figure 10), except in the vicinity of recording sites. The resolution length increases in general toward the periphery of the model.

The most striking feature in the velocity model at shallow depth is a low-velocity anomaly located offshore, adjacent to the main seismogenic areas of the TFZ. This anomaly appears more or less doughnut shaped at shallow depths, indented by a fast anomaly near Grímsey Island. The lowest velocities within the anomaly
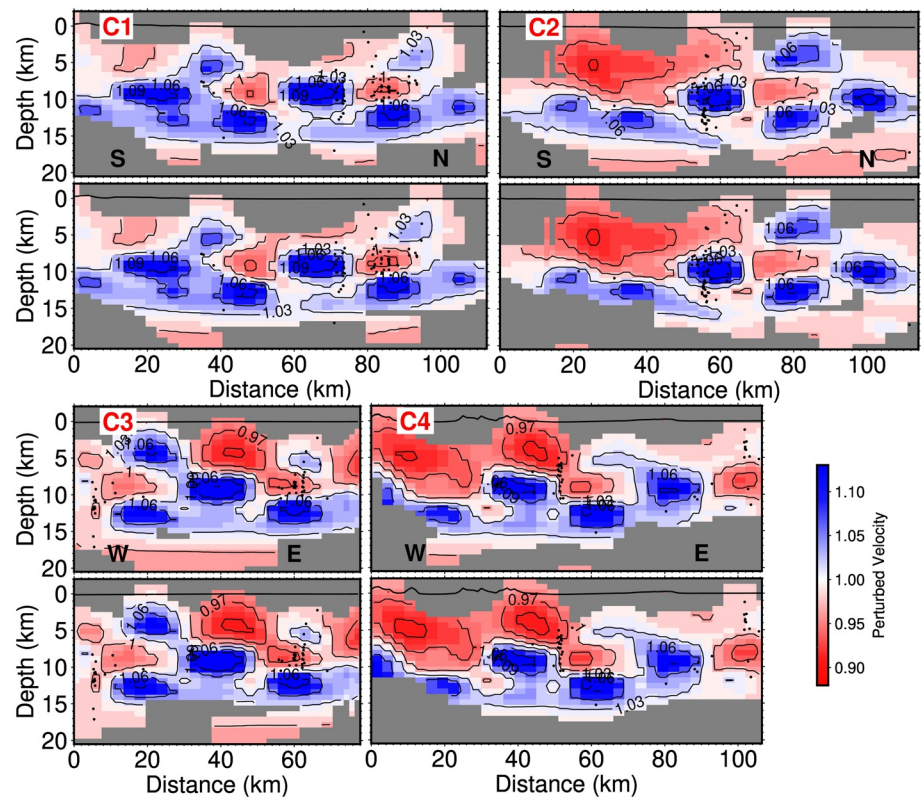
Figure 9. Checkerboard test with checkers also varying in depth with a perturbation of ±5%. Cross-sections at four different locations (see lower-left panel in Figure 8) are presented. Test results at each cross-section are presented for P- (upper panels) and S-waves (lower panels).

align on the northern side of the HFF. At 4.75–5.5 km the anomaly persist, however, at this depth it is most clearly seen on the northern side of the HFF and underneath the volcanic systems Nafir and Mánáreyar in the GOR. The low velocities along the HFF and the GOR are connected in a region extending from Flateyjarskagi Peninsula to the Mánáreyjar volcanic system. In the center of the doughnut, which coincides with Grímsey Island, velocities are high.

Velocities range from above 6.0 km/s (P-wave) and 3.5 km/s (S-wave) in the most-upper crust (mainly above ~3.0 km depth) to nearly 7.0 km/s (P-wave) and 4.0 km/s (S-wave) at depths under 5.5 km. At 7.75–8.50 km depth the P- and S-wave velocities are generally lower offshore than onshore. High velocities occur at this depth also in the northernmost part of the model underneath Stóragrunn. Recorded seismicity is sparse in this area and the velocity structure is primarily constrained by the explosions fired during the NICE experiment. As indicated by the ray coverage plot (Figure 7) the resolution in this area is worse than further to the south.

Localized high-velocity anomalies are present under the tips of the Tröllaskagi, Flateyjarskagi and Tjörnes Peninsulas. Of these, the anomaly beneath Tröllaskagi Peninsula is the clearest at all depths. This volume is well resolved despite its location near the border of the study area due to the two stations located there, one permanent station of the SIL network (sig) and one temporary station, and the abundant seismicity in the ER. The smallest of the named features are nominally resolved according to our model appraisal and resolution analysis. The larger anomalies are clearly resolved. Correlated low velocities for P and S waves were also reported by Riedel et al. (2005) along the HFF at 7–12 km depth, although their resolution is not clearly demonstrated. They also report a NS trending, elongate, low-velocity feature at 7 km depth north of Skjálfandi Bay. Its linear shape is not clear in P-wave velocities and this feature likely corresponds to the low-velocity link we map between Flateyjarskagi and the Mánáreyjar Volcanic System.
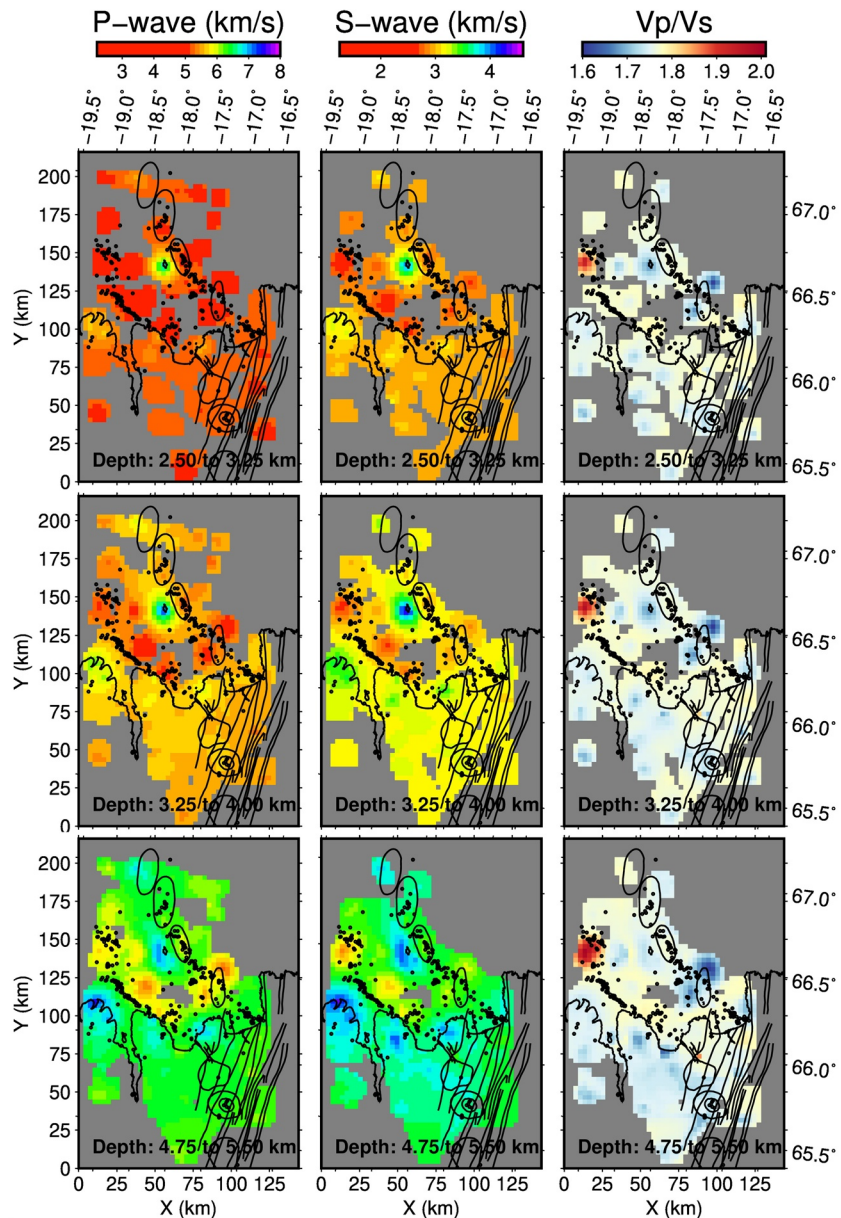
Figure 10. 3-D velocity model from the LET at 2.50–3.25 km, 3.25–4.00 km, and 4.75–5.50 km depth. The panels show map views of the model at different depth intervals. Vp and VS velocity models are presented in the left and central panels, respectively, and the Vp/Vs ratio is shown in the right panels.

Some variations of the Vp/Vs ratio are shown in Figures 10–12. The clearest low Vp/Vs anomaly is located near the northern end of the Mánáreyjar volcanic system east of Grímsey Island. It is localized near the surface and spreads along the GOR to the northwest with increasing depth (e.g., at 7.75–8.5 km depth in Figure 11). The Vp/Vs ratio is close to 1.7. Another low Vp/Vs anomaly of similar amplitude is found at 7.75–8.5 km depth SE of Flatey Island. The most prominent high Vp/Vs anomaly is located in the southern part of Eyjafjarðaráll Basin, where Vp/Vs is ~1.85. A smaller high Vp/Vs anomaly is found along the HFF beneath Flatey Island.

Several of the same features are highlighted in the cross-sections in Figure 12. In profile P1 (along the HFF), the prominent low-velocity anomaly along the HFF is clearly seen at distances between 40 and 80 km as suppressed iso-velocity contours (6.0 and 6.5 km/s for P-wave velocity, and 3.0 and 3.5 km/s for S-wave velocity). Though this anomaly is centered just north of the HFF and not underneath the profile. The low
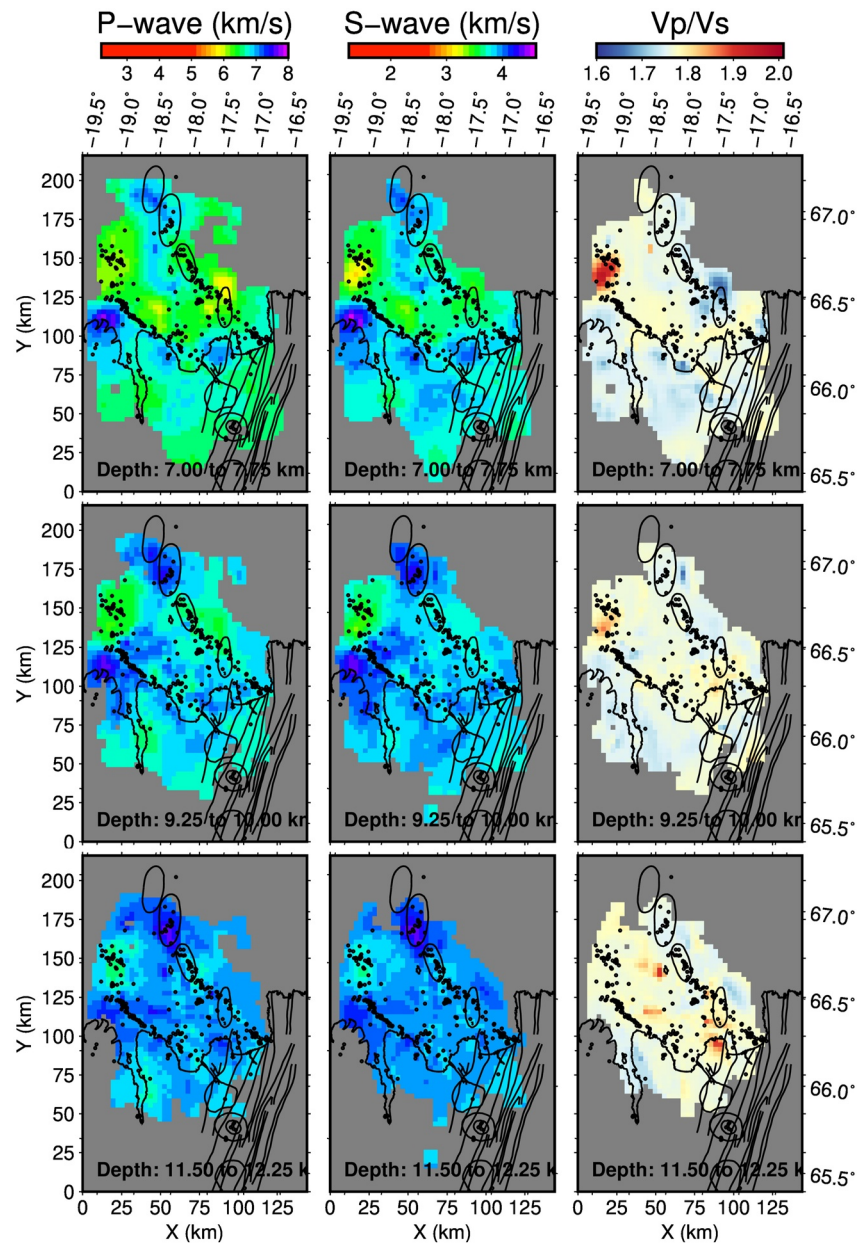
Figure 11. 3-D velocity model from the LET at 7.00–7.75 km, 9.25–10.00 km, and 11.50–12.25 km depth. The panels show map views of the model at different depth intervals. Vp and VS velocity models are presented in the left and central panels, respectively, and the Vp/Vs ratio is shown in the right panels.

Vp/Vs ratio observed at depth near Flatey Island extends and deepens to the NNW underneath the HFF between 40 and 100 km. East of there, the profile lies on land and crosses the Northern Volcanic Zone of Iceland. In that part the structure appears quite homogeneous, with the P-wave 6.5 km/s iso-velocity contour at approximately 5 km depth. At the western end the structure along profile P1 is different. Here, the upper crust (depth to the Vp = 6.5 km/s iso-velocity contour) is similar to the eastern end, but very high velocities, above 7.0 km/s, reach above 10 km depth. This part of the profile crosses the high-velocity anomaly near the northern tip of Tröllaskagi Peninsula, which spreads over a larger area at depth. The velocities reach a slightly higher value further south.

The high Vp/Vs anomaly at Flatey Island appears at 2–5 km depth. Profile P2 lies along the GOR east of Grímsey Island in its eastern half and crosses the northern part of the Grímsey Shoal and the northern part
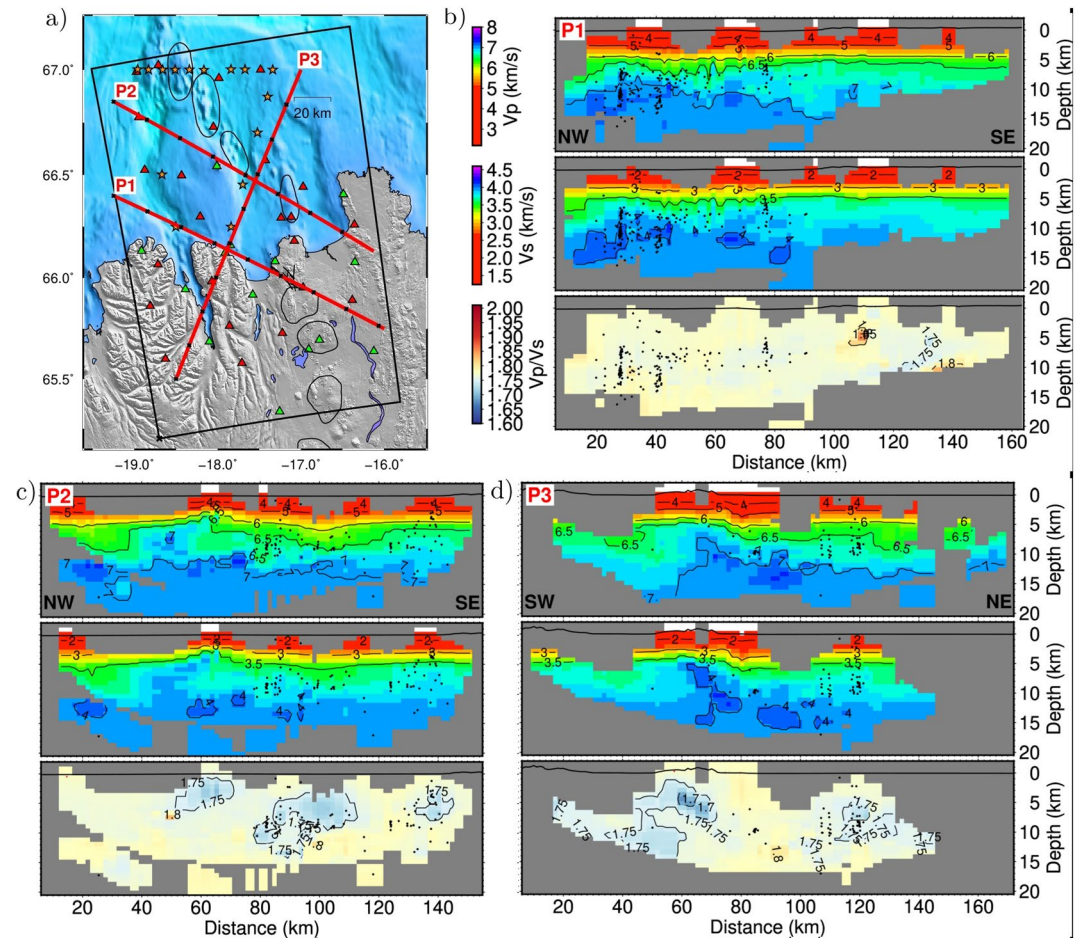
Figure 12. Cross-sections through the study area. (a) Map showing the location of the cross-sections. Black crosses are set every 20 km along the lines. Cross-sections (b) P1, (c) P2, and (d) P3 present the 3-D velocity model for P-waves, S-waves, and the Vp/Vs ratio. The seismicity within ±1 km of the sections are shown as black dots.

of Eyjafjarðaráll Rift to the WNW. At a distance of about 100 km, near the Mánáreyjar volcanic system, the depth to the Vp = 6.0 km/s iso-velocity contour is depressed. The interior of the Grímsey Shoal appears as a high-velocity anomaly at distances between 40 and 60 km. A low Vp/Vs anomaly spreads out along the GOR between the Nafir and Mánáreyjar volcanic systems at 6–12 km depth. A small Vp/Vs low is found near the eastern end of profile P2 where the GOR connects to the Krafla Fissure Swarm. Profile P3 lies transverse to the main lineaments of the TFZ past Flatey Island. It crosses the HFF and profile P1 at about 75 km distance and the GOR and profile P2 at about 110 km. On land, beneath the southernmost third of the profile, the structure is rather homogeneous and similar to the SE end of profile P1 with the P-wave 6.5 km/s iso-velocity contour at about 5 km depth. A sharp change in structure occurs where the profile crosses the HFF close to Flatey Island at about 75 km. Offshore, the depth to the P-wave 6.5 km/s iso-velocity contour is close to 10 km. Just south of the HFF, relatively high velocities reach the near surface. This is a small high-velocity anomaly beneath the Flateyjarskagi Peninsula. A band of low Vp/Vs arcs along the profile at depth. This is clearest at 120 km distance just north of the GOR. This is the anomaly earlier associated with the area in between the Mánáreyjar and Nafir volcanic centers.

4.1. Hypothesis Test

The checkerboard tests described in Section 3.4.1 address the issue of resolution in the tomography in a general sense. Estimating resolution in LET is a difficult task because the locations of both the ray paths and the earthquakes are controlled by the specifics of the velocity models. These effects can be particularly
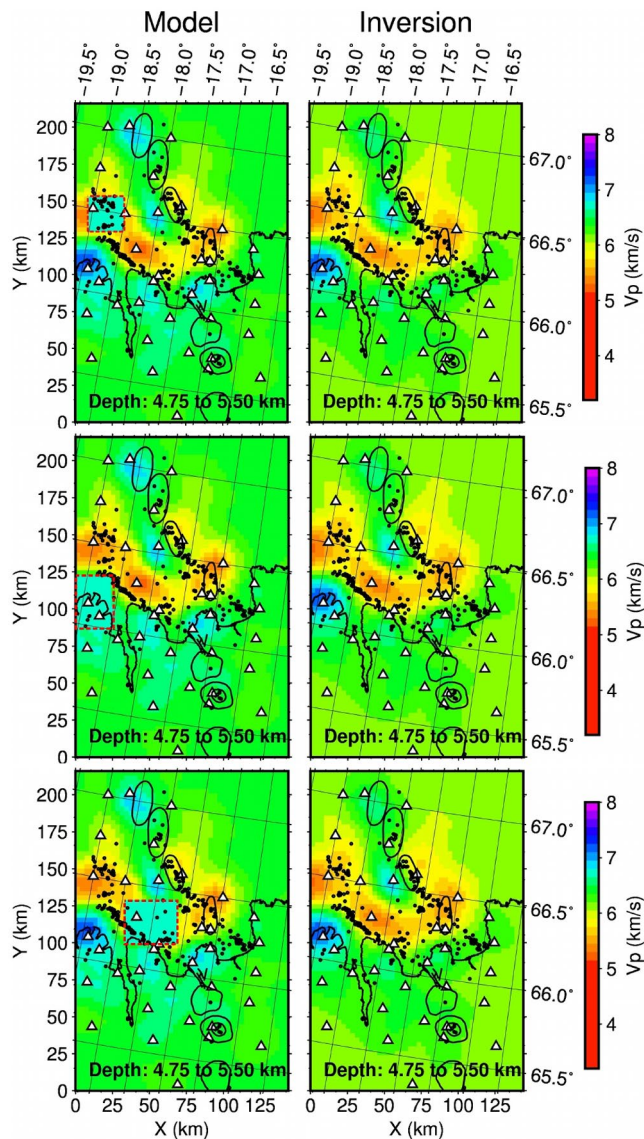
Figure 13. Hypothesis tests removing low-velocity anomalies in the ER and the central HFF, and a high-velocity anomaly beneath Tröllaskagi Peninsula. Left panels show the starting velocity model with the anomaly removed. Red dashed rectangle encloses the removed anomaly. Right panels show the recovered velocity model after reinversion.

strong in a velocity model with a strong small-scale velocity heterogeneity. Our results contain 20% velocity variations in the shallow parts of the model causing both strong lateral and vertical velocity gradients. In order to analyze the robustness of some specific model features, we conducted a series of hypothesis tests.

For these tests, the selected anomalies were removed from the final velocity model by replacing them with a regional velocity average. This model was then used as a starting model for a few more inversion. This procedure allows the inversion to recover the anomaly in the velocity model if it is required by the data. We present tests of three anomalous regions, two regions within the doughnut shaped shallow velocity anomaly offshore, and the high-velocity anomaly beneath Tröllaskagi.

The results are presented in Figure 13. The left panels show the initial P-wave velocity model with a specific anomaly removed from the model. The right panels show the recovered velocity model after inversion. The three tested anomalies are all recovered in shape and amplitude, albeit not in detail. This indicates that the tested anomalies are required by data and are not strongly affected by the specific non-linear effects of the model, giving us confidence to interpret them as realistic features of the crustal structure in the TFZ.

4.2. Bouguer Anomaly

Variations on the crustal velocities can be associated with variations on the density of rocks. A clear gravity low located offshore the Tjörnes Fracture Zone has been reported in the compilation of free-air gravity anomaly by Eysteinsson and Gunnarsson (1995). That motivated us to analyze the gravity in the area and compare it with our tomographic results. To estimate the Bouguer anomaly, we used the free-air gravity data from D. T. Sandwell and Smith (2009), D. Sandwell et al. (2013) and D. T. Sandwell et al. (2014), determined at an altitude of 0 m. Those data were smoothed with a filter of 14 km wavelength (D. Sandwell et al., 2013), and have a resolution of 7 km. The free-air gravity anomaly is overprinted by variations in the topography. Therefore, we corrected it for topographic effects (Forsberg, 2003) applying a Bouguer correction and a terrain correction, using elevation data from Smith and Sandwell (1997). The smoothing filter applied to the free-air gravity anomaly was also applied to the elevation data to reduce the contribution of small-scale anomalies in the Bouguer anomaly. We present the Bouguer anomaly after the described processing in Figure 14a and the detrended anomaly in Figure 14b. In the detrending we have removed the best fitting North/South dipping plane. The removed trend likely includes effects of crustal thinning toward the north and the transition from Icelandic to a more oceanic crust.

The detrended Bouguer anomaly shows a curvilinear feature along the HFF with an axis parallel to and just north of the HFF. It is 10–15 km wide and its amplitude reaches about −40 mGal. Its orientation swings toward the north at the ER and toward the south in Skjálfandi Bay. Additionally, increased gravity values can be found along the axis of the ER (~10 mGal) and at Grímsey Island (~20 mGal), while a gravity low is located north of the Tjörnes Peninsula (just north of 66.5°).

Up to 4 km thick sediments from the Quaternary (Eiríksson et al., 2000; Gudmundsdóttir, 2010; Søndergaard, 2010;) and Holocene (Solomina et al., 2015) periods have been mapped in our study region by Gunnarsson (1998) and Richter and Gunnarsson (2010), and are represented as thickness contours in Figure 14. The sediments are thickest along and north of the HFF, but the negative gravity anomaly is not strongest
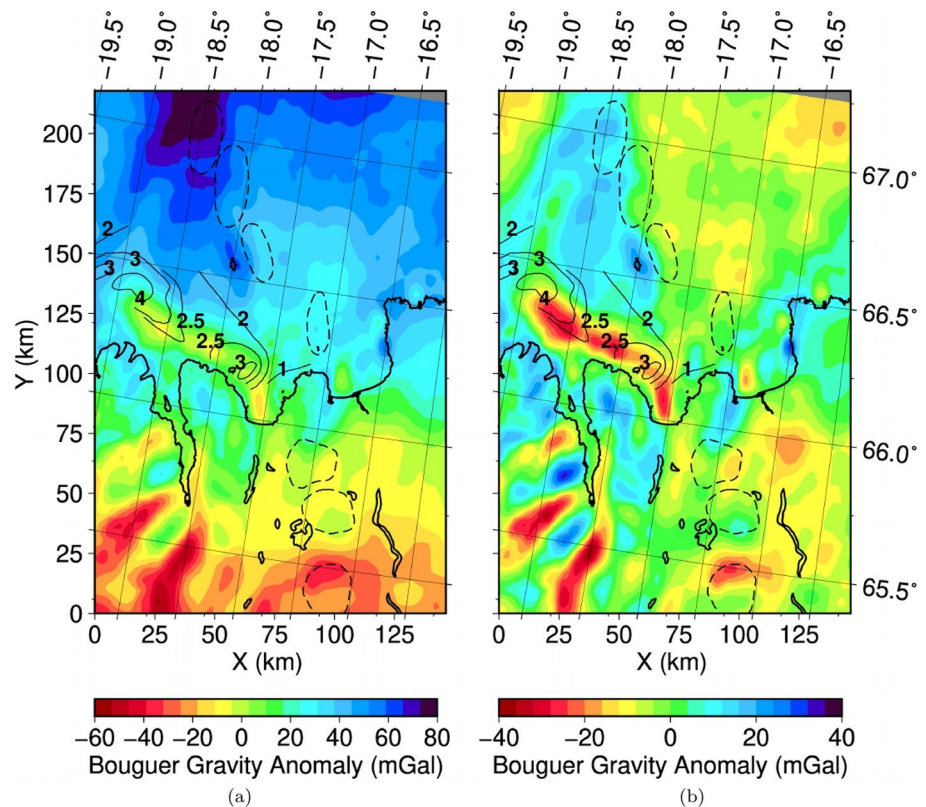
Figure 14. Bouguer anomaly based on D. T. Sandwell and Smith (2009), D. Sandwell et al. (2013) and D. T. Sandwell et al. (2014), and contour lines of sediment thickness estimated by Gunnarsson (1998) (see also Richter and Gunnarsson, 2010). The maps present (a) the Bouguer anomaly and (b) the detrended Bouguer anomaly removing the best fitting, northward, linear trend.

where the sediments are mapped thickest, and the sediment anomaly extends in a broader area than the gravity anomaly. Of course, the gravity integrates density structures to depth and may at longer wavelengths contain signature of deeper structures, for example, crustal thickness variations.

5. Discussion

One of the more prominent feature in the velocity model is the linear band of low velocities along the northern side of the offshore part of the HFF. This anomaly is about 60 km long, 20 km wide and extends from the southern part of the ER to Skjálfandi Bay. It reaches 5.5 km depth and is well resolved according to the hypothesis tests. Small variations of the Vp/Vs ratio are associated with this anomaly, most notably a small high at Flatey Island, strongest at about 5 km depth. A broader and deeper low Vp/Vs anomaly that is strongest just east of Flatey Island near the ESE end of the anomaly, extends along the fault zone at depth and deepens to the NW (see Figure 12b).

The HFF low velocity anomaly is co-located with a gravity low along the northern side of the HFF (Figure 14). The width of the HFF gravity low suggests that the bulk of its density sources lie above about 5 km depth. If so, its amplitude can be explained with a density contrast up to 500 kg/m^3. This can be a reasonable contrast between Quaternary sediments and volcanic upper-crustal rocks, although the uppermost crust in Iceland is quite porous and characterized by low seismic velocities and relatively low density (Pálmason, 1971). Thus, the crude features of the gravity anomaly could be explained by sediments though the along-strike variations of the sediment thickness do not coincide in detail with variations within the gravity anomaly. As the low velocities continue into the ER, this would require invoking a deeper density high underneath the western end of the sediment distribution. Tentatively, the source of the broad gravity high along the ER may thus continue further to the south and be associated with high velocities observed

under the NW end of Profile 1 (Figure 12b). Perhaps the crust is thinner beneath the ER due to its avolcanic rifting. It should be noted that sediments compact with pressure at depth and 500 kg/m^3 may therefore be a large value for an average over about 5 km. The sediment distribution is generally too broad to explain the narrow gravity anomaly. Also, the velocity anomaly reaches depths that exceed the sediment thickness spread by the finite depth resolution of the tomography (∼3 km). Therefore, we conclude that a part of the low velocities along the north side of the HFF are likely due to the sediments, but the anomaly at depth cannot only be due to smearing of the signature of the sediments to depth. Also, shallow, fresh sediments are expected to posses a high Vp/Vs ratio (Kondilarov et al., 2015). No such systematic anomaly is seen in the tomographic results, only a small, localized, positive anomaly at Flatey Island concentrated at 5 km depth and another in the southern ER.

At greater depth, low velocities are associated with the HFF and GOR (as well as in between them north of Skjálfandi and Tjörnes) to approximately 10 km depth. Similar deep low velocities have been mapped at other oceanic transforms (Van Avendonk et al., 2001; Roland et al., 2012). This may be caused by fracturing of the crustal rocks due to the shearing deformation around the transform or excess hydrous alteration due to water percolating through the fractures from above. If so, one would expect associated density anomalies at depth, which, in turn, would contribute to the broader features of the Bouguer anomalies in Figure 14. Serpentinization of the mantle beneath the fracture zone and subsequent ascent of light serpentinite into the crust (Hensen et al., 2019) is possible given the high density of the lower crust in Iceland (Gudmundsson, 2003), but seems unlikely because of the thickness of the crust (15–20 km (Darbyshire et al., 2000)) as such deep fractures may not be significantly permeable.

Low Vp/Vs ratios are mapped at 5–10 km depth beneath much of the HFF, dipping gently to the WNW (see Figure 12, profile P1). They are not present on land at the ESE end of the profile, where the crustal structure is relatively homogeneous and similar to average Icelandic crust (Flóvenz, 1980; Pálmason, 1971), or at the WNW end of the profile, where the HFF merges with the ER. Fractured rock, saturated with highly compressible fluid, will have a low Vp/Vs ratio (Tryggvason et al., 2002; Wang et al., 2012). Therefore, these anomalies may indicate the presence of supercritical H$_2$O or other compressible fluid. The critical point of water is at approximately 375°C. If this condition is reached at 5 km depth, that would imply a temperature gradient of 75°/km, which is feasible in the Icelandic crust (Flóvenz & Sæmundsson, 1993).

The part of the doughnut shaped low-velocity anomaly in the top 5.5 km of the crust that is located along the HFF is discussed previously. The anomaly extends from the HFF near Flatey Island to the NE and into the GOR and the Mánáreyjar volcanic system (Figures 10 and 11). Low velocities also extend along the GOR toward the NW. The low-velocity anomaly appears to reach the greatest depth near the Nafir and Mánáreyjar volcanic systems (see Figure 12d, profile P2 from 80 to 110 km and profile P3 at ∼120 km). This pattern of low-velocity anomalies resembles the distribution of weak gravity lows (∼10 mGal) in the gravity maps in Figure 14b, although the gravity anomaly extends further north beyond the well-resolved part of the velocity model. Relatively thin sediments are found in this region (Gunnarsson, 1998; Sturkell et al., 1992; Richter & Gunnarsson, 2010) and no clear sediment thickness anomalies are mapped, but information is sparse. This part of the low-velocity anomaly coincides with the strongest low Vp/Vs anomaly in our results, visible along profile P2 at 75–100 km between the Nafir and Mánáreyjar volcanic systems at 5 and 10 km depth (Figure 12c). Its interpretation is not obvious. We speculate that along the GOR the low velocities may relate to the volcanism of the area, and argue that the similarity of the gravity anomaly to the velocity anomaly lends the latter support. The low Vp/Vs ratios may indicate the presence of supercritical fluids within the volcanic systems.

The eye of the doughnut, the high velocities around Grímsey Island, clearly coincide with a local gravity high (∼30 mGal) corroborating the tomographic result. This anomaly appears along profile P2 in Figure 10 at distances between 40 and 60 km as an updoming of the 6.5 km/s P-wave iso-velocity contour. Grímsey Island sits on the Grímsey Shoal comprising the western half of the Tjörnes Microplate which is devoid of seismicity in the SIL catalog. One possible explanation of this anomaly is in terms of shallow cumulates associated with an extinct Tertiary volcanic center, possibly from an earlier configuration of spreading. We also note that about half of the crustal accretion history of Iceland since the reconfiguration of spreading from the Ægir Ridge to the Kolbeinsey Ridge about 30 million years ago is apparently missing in the surface geology of Iceland (Foulger, 2006), due to ridge jumps and the aerial extent of basaltic volcanism. Therefore,

blocks of older crust (15–30 million years old) are hidden underneath younger lava flows. Foulger (2006) argued that this may complicate the distribution of crustal thickness in Iceland and possibly explain low-velocity zones in the middle of the crust (~10 km depth) as light differentiated components (e.g., felsic rocks) concentrated near the surface of these blocks may be buried to significant depth. Likewise, if such a block was heavily eroded, it could explain high mid-crustal velocities in the near surface such as those mapped beneath the Grímsey Shoal.

The high velocities beneath the northern tip of Tröllaskagi Peninsula exceed a P-wave velocity of 7.0 km/s at 5 km depth. This high velocity is difficult to explain at such shallow depth. It is similar to velocities found in the lower crust likely to consist of compressed crystalline intrusives and cumulates possibly with higher olivine content than normal Icelandic crust (Gudmundsson, 2003). Hypothesis testing indicates that this anomaly is well resolved. It is not associated with anomalous Vp/Vs estimates. Some rhyolite is found exposed in the area according to the geological map of Jóhannesson (2014). Therefore, we suggest that this anomaly may relate to a poorly exposed Tertiary volcanic center, i.e., it cumulates beneath a relic shallow magma reservoir similar to the one mapped by Brandsdóttir et al. (1997) beneath Krafla volcano and by Jeddi et al. (2017) at Katla. Similar, but less pronounced high-velocity anomalies underneath the Flateyjarskagi and Tjörnes Peninsulas may have the same explanation. Some correlation with local gravity highs (10–20 mGal) is found in these areas.

High velocities at depth (5–10 km) beneath the NW end of the GOR also coincide with a gravity high which extends to the south along the ER. This may be caused by crustal thinning in the melt starved rift and it is possible that our first-arrival-time tomography is affected by mantle waves (Pn, Sn) although we have not been able to identify any PmP (or SmS) phases to constrain the crustal thickness.

6. Conclusions

A 3-D velocity model for the TFZ has been estimated by LET, using data from the NICE experiment carried out during the summer of 2004. Several velocity anomalies have been identified in the velocity model, which relate to the tectonic elements of this complex transform region.

- The HFF is for much of its length (from its western end to Flatey Island) delineated by a low-velocity anomaly on its northern side that extends to at least 5.5 km depth. A curvilinear gravity low coincides with this anomaly, although the Bouguer anomaly is considerably narrower. Anomalously thick (up to 4 km) Quaternary sediments are found in the same general area. Velocities remain low at greater depth as a part of a larger region in between and including the GOR. We interpret the deeper parts of this velocity anomaly beneath the ESZ as due to fracturing of rocks at depth due to the stress field and motion of this transform segment of the TFZ
- A band of low Vp/Vs anomalies is found along the same segment of the HFF at a depth of 5–10 km. We interpret this feature as due to supercritical fluids in the deep fractures of the segment
- Low velocities are also found along the volcanic northwestern part of the GOR that may relate to anomalous temperatures in the upper crust, for example, due to intrusion, or fracturing of the crust. Low Vp/Vs is also mapped in this region at depth and may again be caused by supercritical fluids (melt is too incompressible to cause a low Vp/Vs ratio)
- The northern part of the Grímsey Shoal appears as a fast anomaly in the upper crust. This may be the signature of a relic Tertiary (Miocene/Pliocene) volcano or an older (Oligocene/early Miocene) eroded crustal block
- Upper crustal velocities are higher on land than at sea. In particular, localized high-velocity anomalies are mapped beneath the Tröllaskagi and Flateyjarskagi Peninsulas. These may be the signatures of relic Tertiary volcanic centers with which exposed rhyolites are associated

Data Availability Statement

Datasets for this research are available in Abril et al. (2020). Waveforms recorded by the SIL network in North Iceland, from May–August 2004, are only available under request to the Icelandic Meteorological Office (https://en.vedur.is/about-imo/contact/). Waveforms recorded by the OBSs deployed during the NICE project are available under direct request to the Pr. Dr. Torsten Dahm (torsten.dahm@gfz-potsdam.de).

References

Abril, C., Gudmundsson, O., & the SIL seismological group. (2018). Relocating earthquakes with empirical traveltimes. *Geophysical Journal International*, *214*(3), 2098–2114. https://doi.org/10.1093/gji/ggy246

Abril, C., Tryggvason, A., Gudmundsson, O., & Steffen, R. (2020). Database of earthquake locations (summer 2004), Bouguer gravity anomaly, and P- and S-wave 3-D velocity models of the Tjörnes Fracture Zone (North Iceland). https://uppsala.app.box.com/s/3df9bye08d-d0w3keyyksrwycl1dn1li7 [Online; accessed 6 June 2020].

Aster, R., Borchers, B., & Thurber, C. (2005). In R. Domowska, J. R. Holton, & H. T. Rossby (Eds.), *Parameter estimation and inverse problems. International Geophysics Series 90*. Burlington: Elsevier Academic Press.

Bodvarsson, R., Rognvaldsson, S., Jakobsdottir, S., Slunga, R., & Stefansson, R. (1996). The SIL data acquisition and monitoring system. *Seismological Research Letters*, *67*(5), 35–46. https://doi.org/10.1785/gssrl.67.5.35

Bödvarsson, R., Rögnvaldsson, S., Slunga, R., & Kjartansson, E. (1999). The SIL data acquisition system—At present and beyond year 2000. *Physics of the Earth and Planetary Interiors*, *113*(1–4), 89–101.

Brandsdóttir, B., Menke, W., Einarsson, P., White, R., & Staples, R. K. (1997). Färoe-Iceland ridge experiment 2. Crustal structure of the Krafla central volcano. *Journal of Geophysical Research*, *102*(B4), 7867–7886. https://doi.org/10.1029/96jb03799

Darbyshire, F., Priestley, K., White, R., Stefánsson, R., Gudmundsson, G., & Jakobsdóttir, S. (2000). Crustal structure of central and northern Iceland from analysis of teleseismic receiver functions. *Geophysical Journal International*, *143*, 163–184. https://doi.org/10.1046/j.1365-246x.2000.00224.x

Einarsson, P. (2008). Plate boundaries, rifts and transforms in Iceland. *Jökull Journal*, *58*, 35–58.

Eiríksson, J., Knudsen, K., Haflidason, H., & Henriksen, P. (2000). Late-glacial and Holocene paleoceanography of the North Icelandic Shelf. *Journal of Quaternary Science*, *15*(1), 23–42.

Eysteinsson, H., & Gunnarsson, K. (1995). *Maps of gravity, bathymetry and magnetics for Iceland and surroundings, Report OS-95055/JHD-07*. Reykjavik, Iceland: National Energy Authority.

Flóvenz, Ó. (1980). Seismic structure of the Icelandic crust above layer three and the relation between body wave velocity and the alteration of the basaltic crust. *Journal of Geophysics*, *47*(1–3), 211–220.

Flóvenz, O., & Sæmundsson, K. (1993). Heat flow and geothermal processes in Iceland. *Tectonophys*, *225*, 123–138. https://doi.org/10.1016/0040-1951(93)90253-g

Forsberg, R. (2003). *An overview manual for the GRAVSOFT Geodetic Gravity Field Modelling Programs*. National Survey and Cadastre of Denmark.

Foulger, G. (2006). Older crust underlies Iceland. *Geophysical Journal International*, *165*, 672–676. https://doi.org/10.1111/j.1365-246x.2006.02941.x

Gudmundsdóttir, E. (2010). Tephra stratigraphy and land-sea correlations: A tephrochronological framework based on marine sediment cores off North Iceland, Ph.D. thesis. Faculty of Earth Sciences, University of Iceland.

Gudmundsson, O. (2003). The dense root of the Iceland crust. *Earth and Planetary Science Letters*, *206*, 427–440. https://doi.org/10.1016/s0012-821x(02)01110-x

Gunnarsson, K. (1998). *Sedimentary basins of the N-Iceland shelf, Report OS-98014*. Reykjavik, Iceland: National Energy Authority.

Havskov, J., & Ottemöller, L. (1999). SEISAN Earthquake analysis software. *Seismological Research Letters*, *70*, 532–534. https://doi.org/10.1785/gssrl.70.5.532

Hensch, M., Guðmundsson, G., & the SIL monitoring group. (2013). Offshore seismicity with large azimuthal gaps: Challenges for the SIL network. In *Proceedings of the International Workshop on earthquakes in north Iceland*. Húsavík, Iceland.

Hensch, M., Riedel, C., Reinhardt, J., Dahm, T., & NICE-People, T. (2008). Hypocenter migration of fluid-induced earthquake swarms in the Tjörnes Fracture Zone. *Tectonophys*, *447*, 80–94. https://doi.org/10.1016/j.tecto.2006.07.015

Hensen, C., Duarte, J., Vannucchi, P., Mazzini, A., Lever, M., Terrinha, P., et al. (2019). Marine transform faults and fracture zones: A joint perspective integrating seismicity, fluid flow and life. *Frontiers of Earth Science*, *7*(39), 1–29. https://doi.org/10.3389/feart.2019.00039

Hole, J. (1992). Nonlinear high-resolution three-dimensional seismic travel time tomography. *Journal of Geophysical Research*, *97*(B5), 6553–6562. https://doi.org/10.1029/92jb00235

Jeddi, Z., Gudmundsson, O., & Tryggvason, A. (2017). Ambient-noise tomography of Katla volcano, south Iceland. *Journal of Volcanology and Geothermal Research*, *347*, 264–277. https://doi.org/10.1016/j.jvolgeores.2017.09.019

Jóhannesson, H. (2014). *Geological Map of Iceland – Bedrock geology – 1600000*. Reykjavik, Iceland: The Icelandic Institute of Natural History.

Kodaira, S., Mjelde, R., Gunnarsson, K., Shiobara, M., & Shimamura, H. (1997). Crustal structure of the Kolbeinsey Ridge, North Atlantic, obtained by use of ocean bottom seismographs. *Journal of Geophysical Research*, *102 B2*, 3131–3151. https://doi.org/10.1029/96jb03487

Kondilarov, A., Mjelde, R., Flueh, E., & Pedersen, R. (2015). Vp/Vs ratios and anisotropy on the northern Jan Mayen Ridge, North Atlantic, determined from ocean bottom seismic data. *Polar Science*, *9*, 293–310.

Magnúsdóttir, S., Brandsdóttir, B., Driscoll, N., & Detrick, R. (2015). Postglacial tectonic activity within the Skjálfandadjúp Basin, Tjörnes Fracture Zone, offshore Northern Iceland, based on high resolution seismic stratigraphy. *Marine Geology*, *367*, 159–170. https://doi.org/10.1016/j.margeo.2015.06.004

Menke, W., West, M., Brandsdóttir, B., & Sparks, D. (1998). Compressional and shear velocity structure of the lithosphere in northern Iceland. *Bulletin of the Seismological Society of America*, *88*, 1561–1571.

Paige, C., & Saunders, M. (1982). LSQR: An algorithm for sparse linear equations and sparse least squares. *ACM Transactions on Mathematical Software*, *8*, 43–71. https://doi.org/10.1145/355984.355989

Pálmason, G. (1971), Crustal structure of Iceland from explosion seismology, PhD thesis.

Pavlis, G., & Booker, J. (1980). The mixed discrete-continuous inverse problem: Application to the simultaneous determination of earthquake hypocenters and velocity structure. *Journal of Geophysical Research*, *85*(B9), 4801–4810. https://doi.org/10.1029/jb085ib09p04801

Podvin, P., & Lecomte, I. (1991). Finite difference computation of traveltimes in very contrasted velocity models: A massively parallel approach and its associated tools. *Geophysical Journal International*, *105*, 271–284. https://doi.org/10.1111/j.1365-246x.1991.tb03461.x

Richter, B., & Gunnarsson, K. (2010). *Overview of hydrocarbon related research in Tjönes, report project No. 503402*. Reykjavik, Iceland: National Energy Authority.

Riedel, C., Tryggvason, A., Brandsdottír, B., Dahm, T., Stéfansson, R., Hensch, M., et al. (2006). First results from the North Iceland experiment. *Marine Geophysical Researches*, *27*, 267–281. https://doi.org/10.1007/s11001-006-9007-0

Riedel, C., Tryggvason, A., Dahm, T., Stefanson, R., Bodvarson, R., & Gudmundsson, G. (2005). The seismic velocity structure north of Iceland from joint inversion of local earthquake data. *Journal of Seismology*, *9*, 383–404. https://doi.org/10.1007/s10950-005-8721-4

Rögnvaldsson, S., Gudmundsson, A., & Slunga, R. (1998). Seismotectonic analysis of the Tjörnes Fracture Zone, an active transform fault in north Iceland. *Journal of Geophysical Research*, *103*, 117–129. https://doi.org/10.1029/98jb02789

Roland, E., Lizzarralde, D., McGuire, J., & Collins, J. (2012). Seismic velocity constraints on the material properties that control earthquake behavior at the Quebrada-Discovery-Gofar transform faults, East Pacific Rise. *Journal of Geophysical Research*, *117*(B11102). 10961–10981. https://doi.org/10.1029/2012jb009422

Sæmundsson, K. (1973). *Evolution of the axial rifting zone in Northern Iceland and the Tjornes Fracture Zone, Report OSJHD7303*. Reykjavik, Iceland: National Energy Authority.

Sandwell, D., Garcia, E., Soofi, K., Wessel, P., Chandler, M., & Smith, W. (2013). Toward 1-mGal accuracy in global marine gravity from CryoSat-2, Envisat, and Jason-1. *The Leading Edge*, *32*(8), 892–899. https://doi.org/10.1190/tle32080892.1

Sandwell, D. T., Müller, R. D., Smith, W. H. F., Garcia, E., & Francis, R. (2014). New global marine gravity model from CryoSat-2 and Jason-1 reveals buried tectonic structure. *Science*, *346*, 65–67. https://doi.org/10.1126/science.1258213

Sandwell, D. T., & Smith, W. H. F. (2009). Global marine gravity from retracked Geosat and ERS-1 altimetry: Ridge segmentation versus spreading rate. *Journal of Geophysical Research*, *114*, B01. https://doi.org/10.1029/2008JB006008

Smith, W. H. F., & Sandwell, D. T. (1997). Global seafloor topography from satellite altimetry and ship depth soundings. *Science*, *277*, 1957–1962. https://doi.org/10.1126/science.277.5334

Solomina, O., Bradley, R., Hodgson, D., Ivy-Ochs, S., Jomelli, V., Mackintosh, A., et al. (2015). Holocene glacier fluctuations. *Quaternary Science Reviews*, *111*, 9–34. https://doi.org/10.1016/j.quascirev.2014.11.018

Søndergaard, M. (2010). Lateglacial and holocene paleoclimatic fluctuations of the North Icelandic shelf – Foraminiferal analysis, sedimentology and tephrochronology of Core MD99-2275. Ph.D. thesis, Department of Earth Sciences, University of Aarhus.

Stefansson, R. (1979). Catastrophic earthquakes in Iceland. *Tectonophys*, *53*(3–4), 273–278. https://doi.org/10.1016/0040-1951(79)90071-4

Sturkell, E., Brandsdóttir, B., Shimamura, H., & Mochizuki, M. (1992). Seismic crustal structure along the Axarfjörður trough at the eastern margin of the Tjörnes Fracture Zone, N-Iceland. *Jökull Journal*, *42*, 13–23.

Tryggvason, A. (1998). Seismic tomography: Inversion for P- and S-wave velocities, Ph.D. thesis. Uppsala University.

Tryggvason, A., & Bergman, B. (2006). A travel time discrepancy in the Podvin & Lecomte *time3d* finite difference algorithm. *Geophysical Journal International*, *165*, 432–435. https://doi.org/10.1111/j.1365-246x.2006.02925.x

Tryggvason, A., & Linde, N. (2006). Local earthquake (LE) tomography with joint inversion for P- and S-wave velocities using structural constraints. *Geophysical Research Letters*, *33*, L07303. https://doi.org/10.1029/2005gl025485

Tryggvason, A., Rögnvaldsson, S., & Flóvenz, O. (2002). Three-dimensional imaging of the P- and S-wave velocity structure and earthquake locations beneath Southwest Iceland. *Geophysical Journal International*, *151*, 848–866. https://doi.org/10.1046/j.1365-246x.2002.01812.x

Van Avendonk, H., Harding, A., & Orcutt, J. (2001). Contrast in crustal structure across the Clipperton transform fault from travel time tomography. *Journal of Geophysical Research*, *106*(B6), 10961–10981. https://doi.org/10.1029/2000jb900459

Wang, X., Schubnel, A., Fortin, J., David, E., Gueguen, Y., & Ge, H. (2012). High Vp/Vs ratio: Saturated cracks or anisotropic effects? *Geophysical Research Letters*, *39*(L11), 307. https://doi.org/10.1029/2012gl051742